Three-Step Switching Frequency Selection Criteria for the Generalized CLLC-Type DC Transformer in Hybrid AC/DC Microgrid

Huang, Jingjing; Zhang, Xin; Zhang, Zhe

Published in:
IEEE Transactions on Industrial Electronics

Link to article, DOI:
10.1109/TIE.2019.2898625

Publication date:
2020

Document Version
Peer reviewed version

Three-Step Switching Frequency Selection Criteria for the Generalized CLLC-Type DC Transformer in Hybrid AC/DC Microgrid

Jingjing Huang, *Member*, *IEEE*, Xin Zhang, *Member*, *IEEE*, Zhe Zhang, Senior *Member*, *IEEE*

***Abstract*—For hybrid AC/DC microgrids, the widely applied high frequency DC transformer (DCT) is usually scheduled to operate at resonant frequency with 50% duty-cycle based semi-regulated control (DCSR) to ensure the power transmission (PT), improve its power-density and simplify the system-level control. However, for a real DCT, it may exist more than one resonant frequency that exhibit totally different features, which may seriously degrade the PT ability if the inappropriate switching frequency is selected. Meanwhile, the actual values of the DCT inductances and capacitances are also changing with the power, temperature, etc., which may lead to the practical resonant frequency's variation. Thus, how to select the suitable switching frequency to guarantee the PT ability against the parameter variation becomes a challenge. In this paper, three-step switching frequency selection criteria (SFSC) are proposed. A generalized CLLC-type DCT (GCLLC-DCT) model is extracted to make the proposed approach available for the LLC-, CLL-, symmetric CLLC- and asymmetric CLLC-type topologies. For convenience, the definition of the active power transmission ratio (APTR) is introduced to help evaluate the PT ability. First, the number, value and impact variables of the resonant frequency are derived and analyzed in Step I as the preliminary. Afterwards, the optimum resonant frequency is confirmed for the GCLLC-DCT as the criterion based on the APTR in Step II. At last, the criterion in Step III is given to finally determine the switching frequency against the parameter variations. The proposed SFSC method is also validated by the experiments.**

***Index Terms*—CLLC, DC transformer, power transmission (PT), resonant frequency, switching frequency.**

Manuscript received September 15, 2018; revised November 11, 2018; accepted January 12, 2019. This work is supported by ACRF Tier 1 Grant: RG 85/18 and the NTU Start-up Grant for Prof Zhang Xin, as well as is supported by the National Natural Science Foundation of China under Grant 51507138. (Corresponding author: Xin Zhang, e-mail: jackzhang@ntu.edu.sg.)

J. Huang is with the Department of Electrical Engineering, Xi'an University of Technology, Xi'an 710048, China, and also with the School of Electrical and Electronic Engineering, Nanyang Technological University, Singapore 639798 (e-mail: hjj7759@163.com).

X. Zhang is with the School of Electrical and Electronic Engineering, Nanyang Technological University, Singapore 639798 (e-mail: jackzhang@ntu.edu.sg).

Z. Zhang is with the Department of Electrical Engineering, Technical University of Denmark, 2800 Kongens Lyngby, Denmark (e-mail: zz@elektro.dtu.dk).

NOMENCLATURE

ACT	AC Transformer.
DCT	DC Transformer.
BIC	Bidirectional Interlinking Converter.
HFT	High Frequency Transformer.
PT	Power Transmission.
VCG	Voltage Conversion Gain.
SFSC	Switching Frequency Selection Criteria.
GCLLC-DCT	Generalized CLLC-Type DCT.
APTR	Active Power Transmission Ratio.
DCSR	50% Duty-Cycle Based Semi-Regulated Control.
HV	High-voltage.
LV	Low-voltage.
V_{H}	DC voltage at HV side of DCT.
V_{L}	DC voltage at LV side of DCT.
v_{AB} and i_{AB}	HFT voltage and current at LV side respectively.
v_{CD} and i_{CD}	HFT voltage and current at HV side respectively.
v_{in} and i_{in}	HFT input voltage and current respectively.
P_{H}	Power at HV side of DCT.
P_{L}	Power at LV side of DCT.
P_B	Transmitted power.
P_{Bref}	Transmitted power reference.
f_r	Resonant frequency.
ω_{rT}	Resonant angular frequency.
f_s	Switching frequency.
ω_s	Switching angular frequency.
n	Turn ratio of the transformer.
L_{r1}, L_{r2}	Leakage inductances.
L_{m1}, L_{m2}	Magnetizing inductances.
C_{r1}, C_{r2}	Series resonant capacitances.
$*_R$	Rated value of $*$.
$*_A$	Actual value of $*$.
$*_D$	Designed value of $*$.
R_{eqH}, R_{eqL}	Equivalent resistances.
g, Q_1, Q_2, k, h	Intermediate variables.
Z_{in}	Equivalent impedance of HFT.
X_{eq}	Equivalent reactance of HFT.

R_{eq}	Equivalent resistance of HFT.
f_{r1}, f_{r2}, f_{r3}	Specific resonant frequencies.
ω_{rT1}, ω_{rT2}, ω_{rT3}	Specific resonant angular frequencies.
P	Active power.
Q	Reactive power.
$\zeta\%$, $\xi\%$	Possible variation ranges of the resonant inductances and capacitances, respectively.
A_{PTR}	Value of APTR.
A_{PTR}^{*}	Desired value of APTR.
m	Number of the resonant frequency.

I. Introduction

Along with the increasing renewable DC sources and DC loads, the DC microgrid becomes popular in recent years [1]. However, its AC power from wind turbine and utility grid needs multiple AC/DC conversion steps to support the DC load, resulting in additional power loss and increased complexity of the DC microgrid [2]. Hence, the co-existing AC and DC sources form the hybrid AC/DC microgrid to improve system compatibility [3], [4].

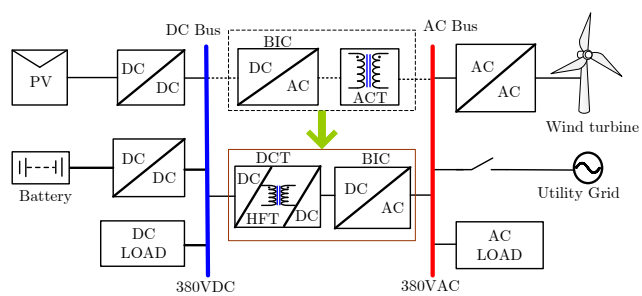

Fig. 1. A typical hybrid AC/DC microgrid.

Fig.1 depicts a typical hybrid AC/DC microgrid [3]-[8]. The line frequency AC transformer (ACT) is deployed in [3] to realize the galvanic isolation and to match the voltage-grade. However, the bulky ACT hinders the efficiency and power-density of the hybrid AC/DC microgrid [5], [6]. Therefore, the high frequency DC transformer (DCT) has been proposed to replace the bulky ACT in the microgrid application to reduce weight and space occupation [7], [8].

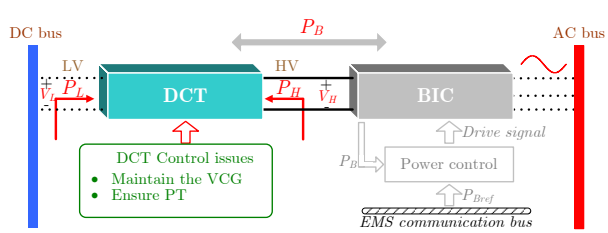

Fig. 2. Cooperation between the DCT and BIC.

In hybrid AC/DC microgrid application, DCT and bidirectional interlinking converter (BIC) must work together to improve the energy utilization by transferring the power between the AC bus and the DC bus [8]. As depicted in Fig. 2, where $V_{\mathrm{H}}(V_{\mathrm{L}})$ & P_{H} (P_{L}) represent the DC voltage & power in the high-voltage (HV) side (low-voltage (LV) side) respectively, DCT and BIC are collaborated in the following way:

- The BIC is responsible of regulating the transmitted power (P_B in Fig. 2) between the AC bus and the DC bus. Its power reference P_{Bref} is achieved through communication bus of the energy management system (EMS) [9], [10]. This is a mature technique, and thus not further discussed here.
- Two main tasks must be realized in DCT. One is to guarantee the power transmission (PT) ability to cooperate with BIC to achieve the high efficiency. Another one is to maintain the voltage conversion gain (VCG), i.e., keep its HV voltage (i.e., V_H in Fig. 2) within the permitted range to ensure the well operation of BIC [8], [11].

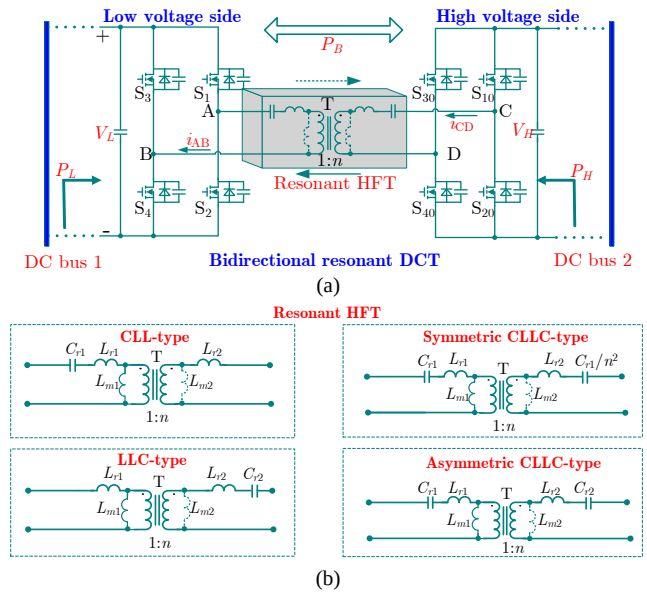

Fig. 3. Typical resonant DCT topology. (a) DCT; (b) Resonant HFT.

A typical DCT topology is depicted in Fig. 3(a), which involves two H-bridge converters and one resonant high frequency transformer (HFT) to reduce the operating power loss and to improve the power-density [8], [12], [13]. Based on the resonant HFT topologies shown in Fig. 3(b), the DCT can be classified as CLL-, LLC-, symmetric CLLC- and asymmetric CLLC-DCT [14]-[16]. Actually, all these resonant DCT topologies can be explained with a generalized CLLC-DCT (GCLLC-DCT) model. However, there are rare reports to discuss the CLL-, LLC-, symmetric CLLC-, and asymmetric CLLC- DCT with a unified form.

For traditional applications such as electric vehicle (EV) [17], battery charging/discharging [18], etc., the DCT is generally designed with wide voltage conversion gain (VCG) to operate as an independent converter system. Therefore, the closed-loop control scheme is essential to regulate DCT to its target voltage/power [19]-[21], which makes the DCT very robust to the parameter variations. However, since P_B is already regulated by the BIC, and the LV side voltage of DCT is maintained by the DC sub-grid in the hybrid AC/DC microgrid application, the relatively complex closed-loop control is not essential for DCT at high-frequency operation. Thus, the

control algorithm of the DCT is required to be as simple as possible to reduce the communication among the DCT, BIC and EMS and to simplify the systematic control. [8], [22].

Therefore, in the microgrid application, the 50% duty cycle based semi-regulated (DCSR) control is usually recommended for the DCT [8], [23]. However, the DCSR controlled GCLLC-DCT challenges the resonant parameters design regarding the PT and VCG. Therefore, a robust parameter design approach is presented in [24] to guide the design of the symmetric CLLC-DCT. This approach can guarantee the desired VCG in the full power range to against the parameter variations. However, when it is applied in the GCLLC-DCT, the PT ability should be further improved to deal with the following problems:

- There may exist more than one resonant frequency f_r for the GCLLC-DCT, which is not discussed in depth [24]. Besides, the value of f_r derived in [23] and [24] is also not accurate enough for the GCLLC-DCT due to the magnetizing inductance is ignored in the symmetric CLLC-DCT. Thus, the number, accurate value and impact variables of f_r should be further derived and discussed.
- The PT ability of the resonant DCT may be seriously degraded at the mismatched f_r, especially when f_r varies with the changing resonant parameters. Therefore, how to determine the optimum f_r from its available values should be further theoretically analyzed.
- It is known that the switching frequency f_s is generally selected as f_s=f_r for the DCT to cooperate with BIC to ensure the PT ability [8], [24]. However, the f_s is constant in the DCSR controlled DCT, while the f_r varies in practice. So, how to finally confirm f_s should be discussed to eliminate the negative impact induced by the mismatch between f_s and f_r.

Therefore, three-step switching frequency selection criteria (SFSC) are proposed in this paper for the GCLLC-DCT. By establishing the general model, the active power transmission ratio (APTR) is introduced to evaluate the PT ability. Afterwards, the number, value and impact variables of the resonant frequency are derived as the preliminary. Also, the switching frequency is selected via considering the APTR characteristics under the different resonant frequency and the resonant parameter variations in practice. The rest of this paper is presented as: Section II establishes the general model of the resonant DCT and presents the problems induced by the parameter variations. The proposed SFSC is detailedly analyzed in Section III. The experimental results of Section IV further verify the theoretically analysis correctness. Conclusion is presented in Section V.

II. General Model And Problem Description of the Resonant DCT

A. General model of the resonant DCT

a) General topology of the resonant DCT

The DCT analysis is actually its HFT analysis. When the power transmits between the LV side and the HV side, the equivalent topology of the resonant HFT circuit is depicted in Fig. 4 (a) and (b). Its circuit parameters are arranged as:

- Turn ratio of the transformer: n.
- Resonant capacitances: C_{r1} and C_{r2}.
- Magnetizing inductances: L_{m1} and L_{m2}.
- Leakage inductances: L_{r1} and L_{r2};
- Equivalent resistances: R_{eqH} and R_{eqL}, whose expressions are as follows:

$$R_{\mathrm{eq}H} = v_{CD} / i_{CD} \,|_{p_{L\to H}} = 8V_H^2 / (\pi^2 P_H) \tag{1a}$$

$$R_{\mathrm{eq}L} = v_{AB} / i_{AB} \,|_{p_{H\to L}} = 8V_L^2 / (\pi^2 P_L) \tag{1b}$$

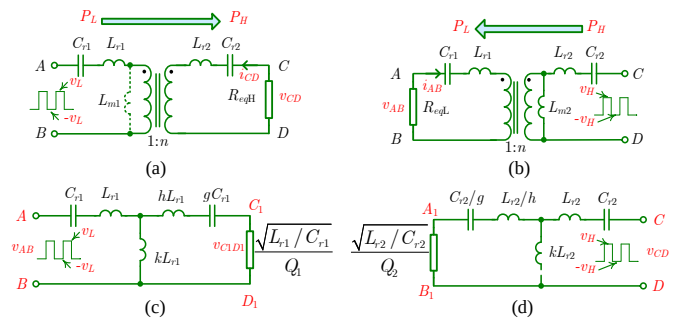

Fig. 4. Equivalent topology of the resonant HFT when power is transmitted: (a) with LV→HV; and (b) with HV→LV. General topology of the resonant HFT when power is transmitted (c) with LV→HV; (d) with HV→LV.

In order to make the topology in Fig. 4(a) and (b) available for the CLL-, LLC-, symmetric CLLC-, and asymmetric CLLC-DCT, the "intermediate variables" g, Q_1, Q_2, k and h are introduced, with the expressions listed below:

$$g = n^2 C_{r2} / C_{r1} \tag{2a}$$

$$Q_1 = n^2 \sqrt{L_{r1} / C_{r1}} / R_{eqH} \tag{2b}$$

$$Q_2 = \sqrt{L_{r2} / C_{r2}} / (n^2 R_{eqL}) \tag{2c}$$

$$k = L_{m1} / L_{r1} = L_{m2} / L_{r2} \tag{2d}$$

$$h = L_{r2} / (n^2 L_{r1}) \tag{2e}$$

For the commonly used transformer, L_{r2}/n^2=L_{r1}, and thus h=1 here. The value of g can be utilized to denote the different resonant DCT topologies:

- When g→0, LLC-DCT will be introduced.
- When g=1, symmetric CLLC-DCT will be achieved.
- When g=C_{st} and C_{st}≠1, where C_{st} is a positive constant, asymmetric CLLC-DCT will be obtained.
- When g→∞, CLL-DCT will be employed.

Therefore, Fig. 4(c) and (d) can be regarded as the general model of the resonant DCT. In the following, CLL-, LLC-, symmetric CLLC- and asymmetric CLLC-DCT can be unified as GCLLC-DCT.

b) Mathematical model of the GCLLC-DCT

When the power transfers from AB(CD) to CD(AB) port, the topology in Fig. 4 can be simplified as Fig. 5. The equivalent impedance Z_{in} can be expressed as

$$Z_{in} = v_{in} / i_{in} = R_{eq} + jX_{eq} \tag{3}$$

where v_{in} and i_{in} indicate the equivalent input voltage and current of the GCLLC-HFT; X_{eq} and R_{eq} denote the equivalent reactance and resistance, respectively.

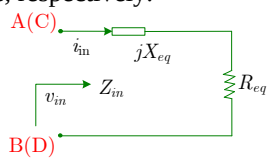

Fig. 5. Simplified topology of the GCLLC-HFT.

- *X_{eq} and R_{eq} expressions with LV→HV power flow*

According to Fig. 4(c), $X_{\rm eq}$ and $R_{\rm eq}$ can be derived as

$$X_{eq}(L_{r1},L_{m1},C_{r1},\omega_s)\,|_{AB\to CD} = L_{r1}^3C_{r1}^2(\sigma_1\omega_s^6+\sigma_2\omega_1^2\omega_s^4+\sigma_3\omega_1^4\omega_s^2-\omega_1^6)\,/\,(\Upsilon\omega_s) \tag{4a}$$

$$R_{eq}(L_{r1},L_{m1},C_{r1},\omega_s)\,|_{AB\to CD} = \omega_s^4R_HL_{m1}^2g^2C_{r1}^2\,/\,\Upsilon \tag{4b}$$

where $\omega_s=2\pi f_s$, and f_s denotes the switching frequency,

$$\omega_1 = 1\,/\,\sqrt{L_{r1}C_{r1}} \tag{5a}$$

$$\Upsilon = {\rm R}_H^2\omega_s^2g^2C_{r1}^2+(\omega_s^2gC_{r1}L_{r1}+\omega_s^2gC_{r1}L_{m1}-1)^2 \tag{5b}$$

$$\sigma_1 = g^2(1+k)(1+2k)\,(>0) \tag{5c}$$

$$\sigma_2 = g^2(1+k)(1\,/\,Q_1^2-1-k)-g(4k+2+k^2) \tag{5d}$$

$$\sigma_3 = (1+2g)(1+k)-g^2\,/\,Q_1^2 \tag{5e}$$

- *X_{eq} and R_{eq} expressions with HV→LV power flow*

The mathematical model when the power is transmitted with HV→LV is the same as that the power transmitted with LV→HV except for replacing $C_{\rm r1}$, $L_{\rm r1}$, Q_1 and g by $C_{\rm r2}$, $L_{\rm r2}$, Q_2 and $1/g$ correspondingly. Hence, it is not further discussed here.

B. Problem description of the GCLLC-DCT

a) Evaluation index of the PT ability for the GCLLC-DCT

According to (3), by letting the imaginary part equal to zero, i.e., $X_{eq}=0$, the f_s can be derived as:

$$f_s = f_r = \omega_s\,/\,2\pi = \omega_{rT}\,/\,2\pi \tag{6}$$

where ω_{rT} is the resonant angular frequency. This also means the reactive power Q is zero, i.e.,

$$P\,/\,\sqrt{P^2+Q^2}=1 \tag{7}$$

where P indicates the transmitted active power in GCLLC-DCT.

If (7) is hold, the following merits will be obtained:

- The unnecessary reactive power can be eliminated to reduce the conduction loss and to decrease the withstand voltage on the resonant capacitors [8].
- It can ensure the high efficiency and good PT ability of the DCT to cooperate with BIC in microgrid applications.

Therefore, the PT ability can be evaluated by the active power transmission ratio (APTR), which is defined as:

$$A_{PTR} = P\,/\,\sqrt{P^2+Q^2} \triangleq R_{eq}\,/\,\sqrt{{X_{eq}}^2+{R_{eq}}^2}\quad(\le 1) \tag{8}$$

where, the desired range of A_{PTR} is defined as:

$$A_{PTR}\in[A_{PTR}^*,1] \tag{9}$$

here A_{PTR}^* relies on the real system requirement.

b) PT Problem induced by parameter variations in practice

- *Parameter variations in practice*

For convenience, a unified form is introduced to define the variation ranges of the actual inductances and capacitances in this paper:

$$L_{\rm xA}\in\left[(1-\zeta\%),\ (1+\zeta\%)\right]L_{\rm xR} \tag{10a}$$

$$C_{\rm xA}\in\left[(1-\xi\%),\ (1+\xi\%)\right]C_{\rm xR} \tag{10b}$$

where L_x represents L_{r1}, L_{r2}, L_{m1} and L_{m2}; C_x represents C_{r1} and C_{r2}. $\zeta\%$ and $\xi\%$ indicate variation ranges of the L_x and C_x; L_{xR} and C_{xR} are the designed value of the L_x and C_x at the rated temperature & power status; L_{xA} and C_{xA} denote the actual value of L_x and C_x, respectively.

An example GCLLC-DCT in [24] is given in Table I to estimate the problems induced by the parameter variations.

TABLE I.
PARAMETERS OF AN EXAMPLE GCLLC-DCT

Items	L_{r1}	L_{r2}	L_{m1}	L_{m2}	Rated power	n	$V_L(V_H)$	C_{r1}	C_{r2}
Values	56μH	223μH	1.4mH	5.6mH	6kW	2	380(760)V	45nF	11nF

Fig. 6 depicts the measured parameters deviation percentage of the example GCLLC-DCT. It can be observed that, the values of inductances and capacitances are changing in practice. This is consistent with the definition in [24].

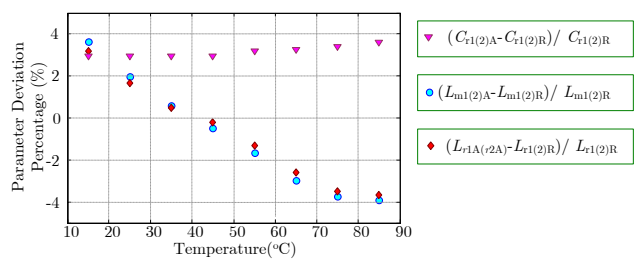

Fig. 6. Scheme of parameter variations vs temperature.

- *PT problem induced by the parameter variations under the mismatched f_r*

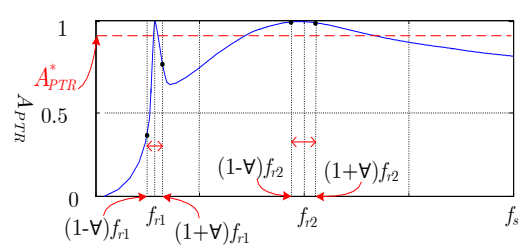

Fig. 7. Schematic diagram of A_{PTR} vs f_s.

It is known that more than one resonant frequency f_r are available for the GCLLC-DCT, and the changing inductances and capacitances make f_r vary online. However, for the resonant DCT, its switching frequency f_s is constant in the 50% duty cycle based semi-regulated (DCSR) control. Therefore, a typical schematic diagram of A_{PTR} vs f_s with two resonant frequencies f_{r1} and f_{r2} is depicted in Fig. 7, where $f_{r1(2)}$ varies

within [1−∀, 1+∀]$f_{r1(2)}$ due to the actual parameters change in practice, and ∀ depends on parameter variation ranges in (10).

It can be observed from Fig. 7 that the slight change of f_{r1} seriously decreases the A_{PTR}. This also means if the inappropriate f_r is employed to cope with the parameter variations, the GCLLC-DCT may lose its PT ability, even resulting the failure cooperation with BIC.

- *PT problem induced by the parameter variations under the different f_s selection*

In the DCSR controlled GCLLC-DCT, the f_s is usually selected as f_s=f_{rR}, where f_{rR} is the resonant frequency achieved at the rated power [23], [24]. However, when operating under the light-load condition, the conventional f_s selection approach may lower the PT ability. To verify this, the waveforms of v_{in} & i_{in} (i.e., v_{AB} & i_{AB}) of the example GCLLC-DCT are given in Fig. 8(a) and (b) with f_s<f_{rR} and f_s=f_{rR} respectively at the light-load condition to compare the PT ability against the parameter variations. It can be observed from Fig. 8(a) that v_{in} and i_{in} are basically kept in phase, while in Fig. 8(b), the v_{in} is ahead of i_{in}.

Since the efficiency directly reflects the PT ability of the GCLLC-DCT, it has been measured in Fig. 8(c), which demonstrates Fig. 8(a) can ensure the higher efficiency.

Therefore, the conventional f_s selection at the rated power may lower the efficiency during the light-load condition, as verified in Fig. 8. It should be further improved to guarantee the PT ability (i.e., APTR) to against parameter variations.

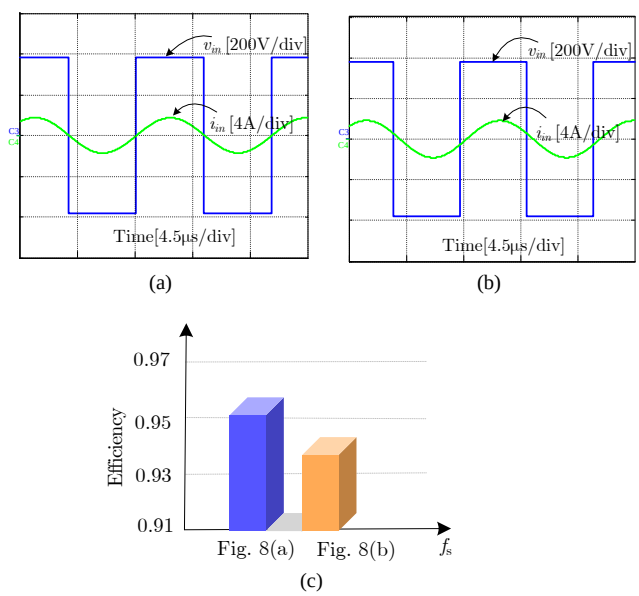

Fig. 8. Waveforms of v_{in} & i_{in} and corresponding efficiency at the light-load condition: (a) f_s <f_{rR}; (b) f_s =f_{rR}; (c) Efficiency.

C. Motivation

The mismatch between f_r and f_s is inevitable in the DCSR controlled GCLLC-DCT of the hybrid AC/DC microgrid application. Therefore, the PT ability (i.e., APTR) may be seriously degraded if the inappropriate f_s is selected to cope with the problems induced by the multiple f_r and the changing resonant parameters. As a result, a three-step SFSC is proposed for the GCLLC-DCT to make (9) hold with the highest possibility to eliminate the negative impact induced by the mismatch between f_r and f_s, with details summarized in Fig. 9.

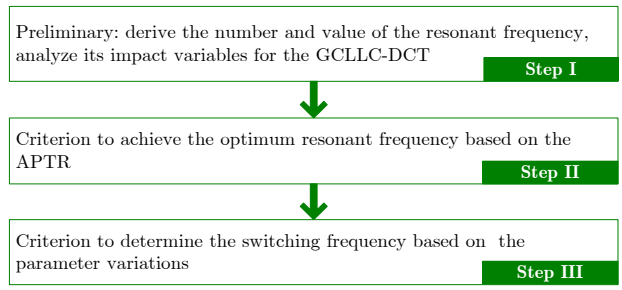

Fig. 9. Flowchart of the proposed three-step SFSC.

III. Proposed Three-Step SFSC of GCLLC-DCT

In this section, the proposed three-step SFSC of the GCLLC-DCT will be presented detailedly. For step I, the number, value and impact variables of the resonant frequency will be analyzed in Section III-A. Step II presents the criterion to achieve the optimum resonant frequency based on the APTR in Section III-B. Afterwards, in Section III-C, the criterion to determine the switching frequency is confirmed based on the parameter variations as step III. At last, a design example is given in Section III-D to facilitate the procedure of the proposed three-step SFSC.

A. Preliminary: the number, value and impact variables of f_r in the GCLLC-DCT

a) Number of f_r in the GCLLC-DCT

According to Section II-B, the highest A_{PTR} in (8) can be achieved by letting the reactive part to be zero, i.e.,

$$X_{eq}(L_{r1}, L_{m1}, C_{r1}, \omega_s)\,|_{AB\to CD} \triangleq F(\omega_s) = y_1 - y_2 = 0 \tag{11a}$$

where

$$y_1 = \sigma_1\omega_s^4 + \sigma_2\omega_1^2\omega_s^2 + \sigma_3\omega_1^4 \tag{11b}$$

$$y_2 = \omega_1^6 \,/\, \omega_s^2 \tag{11c}$$

Eqn. (11a) can be guaranteed by (6), i.e., $\omega_s = \omega_{rT}$ can be achieved at y_1=y_2. Since σ_1>0 (see 5(c)), there are four cases based on the plus-minus of σ_2 and σ_3, as indicated in Table II.

TABLE II.

CASE STUDIES TO ACHIEVE y_1=y_2

CASE	$\sigma_2 \leqslant 0$	$\sigma_2 > 0$
$\sigma_3 \geqslant 0$	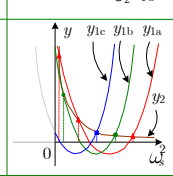 Case I m=3 @ y_1=y_{1a} m=2 @ y_1=y_{1b} m=1 @ y_1=y_{1c}	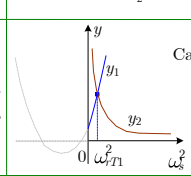 Case III m=1
$\sigma_3 < 0$	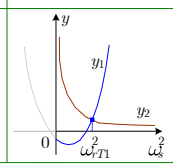 Case II m=1	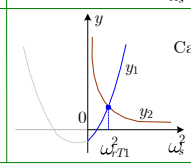 Case IV m=1

NOTE: m denotes the number of f_r and ω_{rT} .

For case I, it can be observed from Table II that, the number of f_r (or ω_{rT}), defined as m, involves three conditions to guarantee $y_1=y_2$:

- m=3 @ $y_1=y_{1a}$, i.e., three resonant angular frequencies ω_{rT1}, ω_{rT2} and ω_{rT3} ($\omega_{rT1}<\omega_{rT2}<\omega_{rT3}$) can be obtained.
- m=2 @ $y_1=y_{1b}$, i.e., two resonant angular frequencies ω_{rT1} and ω_{rT2} ($\omega_{rT1}<\omega_{rT2}$) can be acquired.
- m=1 @ $y_1=y_{1c}$, i.e., only one resonant angular frequency ω_{rT1} can be achieved.

For case II, III and IV, m=1, i.e., there is only one resonant angular frequency ω_{rT1} to make $y_1=y_2$ hold.

The values of ω_{rT1}, ω_{rT2} and ω_{rT3} for the case I~IV are further derived in the following.

b) Value of f_r in the GCLLC-DCT

Eqn. (11a) can be rewritten as

$$F(x)=\sigma_1 x^3+\sigma_2\omega_1^2 x^2+\sigma_3\omega_1^4 x-\omega_1^6=0 \quad (x=\omega_s^2) \tag{12}$$

It can be observed that (12) is a typical cubic equation, which can be solved by the corresponding mathematical approach [25]. To facilitate the procedure for deriving the value of ω_{rT} in case I~IV, the following definitions are given:

$$\mathrm{A}=\sigma_2^2-3\sigma_1\sigma_3 \tag{13a}$$

$$\mathrm{B}=\sigma_2\sigma_3+9\sigma_1 \tag{13b}$$

$$\mathrm{C}=\sigma_3^2+3\sigma_2 \tag{13c}$$

$$\Delta=\mathrm{B}^2-4\mathrm{AC} \tag{13d}$$

- If m=3, i.e., (13d) satisfies

$$\Delta=\mathrm{B}^2-4\mathrm{AC}<0 \tag{14}$$

The three values of ω_{rT} can be derived as

$$\begin{cases}\omega_{rT1}=\sqrt{X_1} & \mathrm{X}_1=\min(x_1,x_2,x_3)\\ \omega_{rT3}=\sqrt{X_2} & \mathrm{X}_2=\max(x_1,x_2,x_3)\\ \omega_{rT2}=\sqrt{X_3} & \mathrm{X}_3=x_1+x_2+x_3-\mathrm{X}_1-\mathrm{X}_2\end{cases} \tag{15}$$

where

$$x_1=\omega_1^2[-\sigma_2-2\sqrt{A}\cos(\theta/3)]/(3\sigma_1) \tag{16a}$$

$$x_{2,3}=\omega_1^2\{-\sigma_2+\sqrt{A}[\cos(\theta/3)\pm\sqrt{3}\sin(\theta/3)]\}/(3\sigma_1) \tag{16b}$$

$$\theta=\arccos\mathrm{T},\ -1<\mathrm{T}<1 \text{ and } \mathrm{T}=0.5(2A\sigma_2\omega_1^2-3\sigma_1 B)/\sqrt{A^3} \tag{16c}$$

- If m=2, i.e., (13d) satisfies that (A≠0):

$$\Delta=\mathrm{B}^2-4\mathrm{AC}=0 \tag{17}$$

The two values of ω_{rT} can be obtained as

$$\begin{cases}\omega_{rT1}=\sqrt{X_1} & \text{where } \mathrm{X}_1=\min(x_1,x_2,x_3)\\ \omega_{rT2}=\sqrt{X_2} & \text{where } \mathrm{X}_2=\max(x_1,x_2,x_3)\end{cases} \tag{18}$$

where

$$x_1=(-\sigma_2/\sigma_1+B/A)\omega_1^2,\ x_2=x_3=-B\omega_1^2/(2A) \tag{19}$$

- If m=1, i.e., (13) satisfies one of the following conditions:

$$\mathrm{A}=\mathrm{B}=\mathrm{C}=0 \tag{20a}$$

$$\Delta=\mathrm{B}^2-4\mathrm{AC}>0 \tag{20b}$$

If (20a) is satisfied, the value of ω_{rT} can be derived as

$$\omega_{rT1}=\sqrt{x_1}=\sqrt{x_2}=\sqrt{x_3} \tag{21}$$

where

$$x_1=x_2=x_3=-\sigma_2\omega_1^2/(3\sigma_1)=-\sigma_3\omega_1^2/\sigma_2=3\omega_1^2/\sigma_3 \tag{22}$$

Note that (22) is uniquely hold on the premise of $\sigma_2<0$ and $\sigma_3>0$, i.e., case I in Table II.

If (20b) is satisfied, the resonant frequency is achieved as

$$\omega_{rT1}=\sqrt{X_1} \tag{23}$$

where

$$X_1=(-\sigma_2-Y_1^{1/3}-Y_2^{1/3})\omega_1^2/(3\sigma_1) \tag{24a}$$

$$Y_{1,2}=A\sigma_2+3\sigma_1-B\pm\sqrt{B^2-4AC}\ /2 \tag{24b}$$

c) Impact variables of f_r

It can be observed from Section III-A-b that the value of ω_{rT} depends on four unknown variables k, g, ω_1 and Q_1. Therefore, the ranges of k, g, ω_1 and Q_1 are discussed in the following.

For *k*: According to (2d) & (10a), the actual value of k can be derived as:

$$k=L_{m1R}/L_{r1R}=L_{m2R}/L_{r2R} \tag{25}$$

It is noted that both $L_{\mathrm{m1(m2)}}$ and $L_{r1(r2)}$ stem from one magnetic core. Therefore, when GCLLC-DCT is operating within its allowable temperature, the value of k in (25) will be stable.

For *g*: According to (2a) and (10b), the actual value of g is rewritten as:

$$g=n^2C_{r2R}/C_{r1R} \tag{26}$$

Since the resonant capacitors are recommended to select the same material, C_{r1R} and C_{r2R} are varying with the same features. Therefore, the value of g is remained the same at any power & temperature conditions.

For ω_1: According to (5a) & (10), the actual value of ω_1 can be obtained to vary within following range:

$$\omega_1\in\left[\frac{\omega_{1D}}{\sqrt{(1+\zeta\%)(1+\xi\%)}},\ \frac{\omega_{1D}}{\sqrt{(1-\zeta\%)(1-\xi\%)}}\right] \tag{27}$$

where ω_{1D} is the designed value of ω_1 at rated power and temperature.

For *Q*₁: By (2b), the value of Q_1 is inversely proportional to R_{eqH}, and R_{eqH} varies from 0 to its rated value R_{eqHR} based on the transmitted power. Therefore, the range of Q_1 is obtained as

$$Q_1\in[0,\ Q_{1max}] \tag{28}$$

where Q_{1max} can be expressed as:

$$Q_{1\max}\triangleq n^2\sqrt{(1+\zeta\%)L_{r1R}/[C_{r1R}(1-\xi\%)]}/R_{eqHR} \tag{29}$$

Comparably, the variable range of Q_1 is much larger than k, g and ω_1. Therefore, the number and value of ω_{rT} largely depend on Q_1, as analyzed below:

- By substituting (5d) and (5e) into $\sigma_2\le 0$ and $\sigma_3\ge 0$, it can be derived that Case I is hold on condition when Q_1 satisfies

$$Q_1\ge\max[\Re_1(k,g),\ \Re_2(k,g)] \tag{30a}$$

where

$$\Re_1(k,g)=\sqrt{g(1+k)/[k^2(1+g)+2k(g+2)+2+g]} \tag{30b}$$

$$\Re_2(k,g) = g \,/\, \sqrt{(1+2g)(1+k)} \tag{30b}$$

- By substituting (5d) and (5e) into $\sigma_2 \leq 0$ and $\sigma_3 < 0$, Case II exists on the condition that

$$\Re_1(k,g) \leq Q_1 < \Re_2(k,g) \tag{31}$$

- By substituting (5d) and (5e) into $\sigma_2 > 0$ and $\sigma_3 \leq 0$, Case III exists on the premise that:

$$\Re_2(k,g) \leq Q_1 < \Re_1(k,g) \tag{32}$$

- By substituting (5d) and (5e) into $\sigma_2 > 0$ and $\sigma_3 < 0$, Case IV exists on the condition that

$$Q_1 < \min[\Re_1(k,g),\ \Re_2(k,g)] \tag{33}$$

The number and value of ω_{rT} (i.e., $2\pi f_r$) as well as its main impact variable Q_1 are summarized in Table III.

TABLE III.
SUMMARY OF THE NUMBER, VALUE AND MAIN IMPACT VARIABLE Q_1 OF ω_{rT}

Case	Q_1	m	ω_{rT}	Condition
I	(30)	m=3	ω_{rT1}, ω_{rT2}, ω_{rT3} based on (15)	Δ<0
		m=2	ω_{rT1}, ω_{rT2} based on (18)	Δ=0
		m=1	ω_{rT1} based on (21)	A=B=C=0
		m=1	ω_{rT1} based on (23)	Δ>0
II	(31)	m=1	ω_{rT1} based on (23)	Δ>0
III	(32)	m=1	ω_{rT1} based on (23)	Δ>0
IV	(33)	m=1	ω_{rT1} based on (23)	Δ>0

Note: Δ, A, B and C refer to (13).

B. Step II. Criterion based on APTR of the GCLLC-DCT

Substituting (4) into (8), the value of A_{PTR} can be deduced as

$$A_{PTR} = R_{eq} \,/\, \sqrt{X_{eq}^{\ 2} + R_{eq}^{\ 2}} = \frac{1}{\sqrt{Q_1^2(\sigma_1\varepsilon + \sigma_2/\varepsilon + \sigma_3/\varepsilon^3 - 1/\varepsilon^5)^2/(g^4k^4)+1}} \tag{34a}$$

$$\varepsilon = \omega_s \,/\, \omega_1 \tag{34b}$$

According to (34), the optimum ω_{rT} determination is converted to select the optimum value of ε (defined as ε_m) from the possible ω_{rT} in Table III. ε_m is expressed as

$$\varepsilon_m = \omega_{rT} \,/\, \omega_1 \tag{35}$$

Therefore, the criterion based on the APTR is transformed to find ε_m to make the A_{PTR} in (34a) locate within its desired range in (9) with the highest probability (i.e., the maximum shadow zone in Fig. 10 to offset the variation of ε_m).

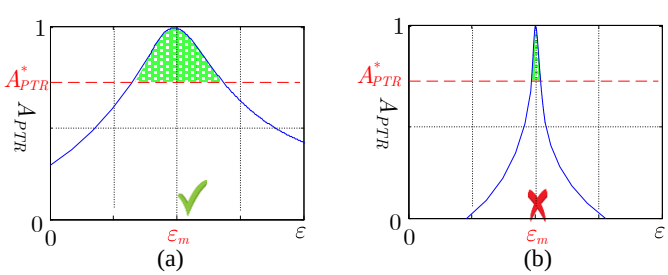

Fig. 10. Schematic of the criterion based on APTR: (a) recommended as ε_m due to the maximum shadow zone; (b) not recommended as ε_m due to the smaller shadow zone.

By (34a), the value of A_{PTR} is related with the selected resonant topologies (i.e., the value of g in Section II-A). Therefore, in the following, the analysis will be carried out based on the topology.

a) g=0, LLC resonant topology

Substituting g=0 into (5c) ~ (5e), it can be derived that

$$\sigma_1 = \sigma_2 = 0,\ \sigma_3 = 1 + k > 0 \tag{36}$$

Therefore, Δ=0 can be achieved based on (13d). According to Table III, two resonant frequencies exist at g=0.

The characteristic of A_{PTR} vs ε is depicted in Fig. 11. Clearly, the range of the desired A_{PTR} around ε_2 is more than ten times wider than that around ε_1. This also indicates that if ε_2 is selected, the permitted variation range of ε will be widest to guarantee the desired A_{PTR}. Therefore, for the LLC-DCT, ε_2, corresponding to the maximum value of ω_{rT}, is recommended due to the highest probability to make $A_{PTR} \in [A^*_{PTR}, 1]$ hold.

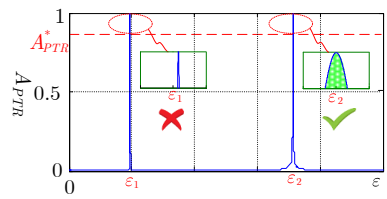

Fig. 11. Characteristic of A_{PTR} vs ε @ g=0.

b) g=1, symmetric CLLC resonant topology

According to Table III, Δ<0, Δ=0, A=B=C=0 and Δ>0 are possible in the symmetrical CLLC-DCT application. By (34), the curves of A_{PTR} vs ε are given in Fig. 12, where ε_3 in Fig. 12(a), ε_2 in Fig. 12(b), and ε_1 in Fig. 12(c), corresponding to the maximum value of ω_{rT}, can ensure the highest probability to achieve the desired A_{PTR}.

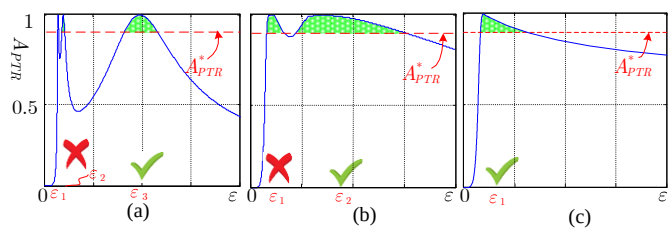

Fig. 12. Characteristics of A_{PTR} vs ε when g=1: (a) m=3; (b) m=2; (c) m=1.

c) g=C_{St}, asymmetric CLLC resonant topology

The characteristics of A_{PTR} vs ε are similar to the results in Fig. 12 obtained by g=1, and thus not further discussed here.

d) g→∞, CLL resonant topology

It can be derived from (5e) that $\sigma_3 < 0$. According to Table I, only case II and IV exist, i.e., m=1 at $g \to \infty$. As given in Fig. 13, only one resonant frequency ε_1 is available.

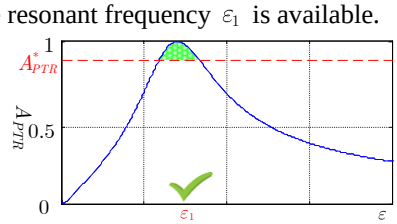

Fig.13. Characteristics of A_{PTR} vs ε @ $g \to \infty$.

The optimum ε_m and corresponding ω_{rT} under the different topologies are summarized in Table IV. It can be concluded from Table IV that, the maximum resonant frequency is recommended as the optimum one to ensure the widest APTR range within $[A^*_{PTR},1]$. This is regarded as the criterion based on APTR for the GCLLC-DCT.

TABLE IV.
RECOMMENDED OPTIMUM ε_m AND CORRESPONDING ω_{rT}

Topology	m	ε_m	ω_{rT}
g→0	m=2	ε_m=ε_2 in Fig. 11	ω_{rT}=ω_{rT2}
g=1(C_{st})	m=3	ε_m=ε_3 in Fig. 12(a)	ω_{rT}=ω_{rT3}
	m=2	ε_m=ε_2 in Fig. 12(b)	ω_{rT}=ω_{rT2}
	m=1	ε_m=ε_1 in Fig. 12(c)	ω_{rT}=ω_{rT1}
g→∞	m=1	ε_m=ε_1 in Fig. 13	ω_{rT}=ω_{rT1}

Note: ω_{rT1}, ω_{rT2} and ω_{rT3} refers to Table III.

C.Step III. Criterion based on the parameter variations of the GCLLC-DCT

The optimum ε_m achieved by the criterion in step II depends on the resonant parameters L_x, C_x, and $R_{eqH(L)}$ (i.e., $Q_{1(2)}$ according to (1)), where L_x represents L_{r1}, L_{r2}, L_{m1} and L_{m2}; and C_x represents C_{r1} and C_{r2}. Therefore, the impacts on ε_m induced by the resonant parameter variations are further discussed below.

a) The impact on ε_m induced by variation of L_x and C_x

In practice, the actual values of L_x & C_x may change with the temperature and power, and thus they are not constant, as stated in Section II-B. According to (10) & (35), the actual ε_m varies within $[\varepsilon_{\min}, \varepsilon_{\max}]$ in practice, and the values of $\varepsilon_{\min}$ and $\varepsilon_{\max}$ are

$$\varepsilon_{\min} = \sqrt{(1-\zeta\%)(1-\xi\%)}\varepsilon_{mD} \tag{37a}$$

$$\varepsilon_{\max} = \sqrt{(1+\zeta\%)(1+\xi\%)}\varepsilon_{mD} \tag{37b}$$

where ε_{mD} is the designed value of ε_m, and can be expressed as

$$\varepsilon_{mD} = \omega_{rT}\sqrt{L_{r1R}C_{r1R}} \tag{38}$$

ω_{rT} refers to Table IV.

b) The impact on ε_m induced by the variation of $Q_{1(2)}$

The characteristics of ε_m vs $Q_{1(2)}$ are depicted in Fig. 14, where ε_m is basically increasing with $Q_{1(2)}$ until it reaches a constant value. According to (1) and (2), it can be achieved that $Q_{1(2)}$ is proportional to the transmitted power. Based on (35), the value of ε_m is up to the value of the optimal ω_{rT}. Therefore, Fig. 14 also indicates the characteristics of ω_{rT} and the transmitted power.

It can be concluded from Fig. 14 that the optimal ω_{rT} is increasing with the transmitted power, and thus the maximum value of ω_{rT} is achieved at the rated power. Therefore, the curves A_{PTR} vs ε under various $Q_{1(2)}$ are depicted in Fig. 15, where the value of ε_m will be decreased when $Q_{1(2)}$ is decreased, and the maximum value of $Q_{1(2)}$ also indicates that the transmitted power is at its rated value. Besides, as observed from Fig. 15, the shadow zone can satisfy $A_{PTR} \in [A^*_{PTR},1]$ for three curves; and only when $\varepsilon = \varepsilon_{\min}$, the highest probability can be guaranteed to make A_{PTR} locate within $[A^*_{PTR},1]$ under the decreasing $Q_{1(2)}$.

In summary, the criterion considering the resonant parameter variations can be summarized as

$$\omega_s = \varepsilon_{\min}\omega_{1D} = \sqrt{(1-\zeta\%)(1-\xi\%)}\omega_{rT} \tag{39}$$

where $\varepsilon_{\min}$ refers to (37a).

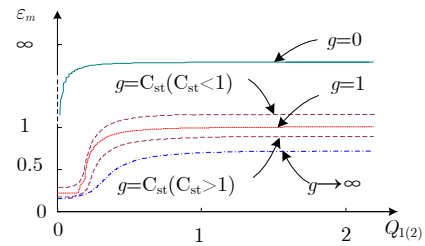

Fig. 14. Characteristics of ε_m vs $Q_{1(2)}$ with g=0, g=1, g=C_{st} and g→∞.

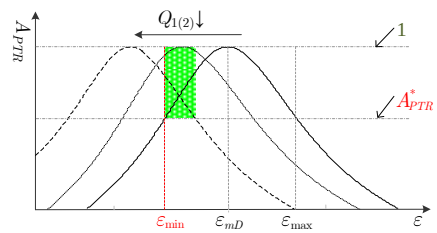

Fig. 15. Characteristics of A_{PTR} vs ε with various $Q_{1(2)}$.

D.Design example

Take the specification of the GCLLC-DCT in Table I as an example to facilitate the proposed SFSC procedure, $\zeta\%$ and $\xi\%$ are 4% according to Fig. 6; k=25 and $Q_1 \in [0, 1.786]$. The f_s will be confirmed in the following steps.

Step I: Calculate the number and value of f_r according to Table III & (6):

- m=3;
- $f_{r1} = \omega_{rT1} / (2\pi) = 14\,\text{kHz}$;
- $f_{r2} = \omega_{rT2} / (2\pi) = 19.6\,\text{kHz}$;
- $f_{r3} = \omega_{rT3} / (2\pi) = 99.75\,\text{kHz}$.

Step 2: Select the maximum value of ω_{rT} based on Table IV:

- $\omega_{rT} = \omega_{rT3}$ are determined, i.e., $f_r = f_{r3} = 99.75\,\text{kHz}$.

It is noteworthy that f_r=99.75kHz determined based on the impedance model is more accurate than the approximate value f_r=100kHz in [24] due to the ignored magnetizing inductance.

Step 3: Confirm f_s based on f_{r3} & (6) & (39):

- $f_s = 95.76\,\text{kHz}$.

These design steps of GCLLC-DCT are derived based on g=1. Adopting the same transformer specification in Table I, the other topologies of the GCLLC-DCT can be achieved by replacing the resonant capacitors as Table V, where the f_s is derived in the same way with the above steps.

To facilitate the f_s selection, a flowchart of the proposed three-step SFSC is given in Fig. 16. Based on the known specifications, the impedance model can be firstly established. By letting the imaginary part of the impedance model to be zero, we can derive the accurate values and number of f_r,

which is also regarded as Step I of the proposed SFSC. After confirming the best f_r based on APTR in Step II, the f_s is finally selected considering both the resonant parameter variations and power variations.

TABLE V.

RESONANT CAPACITORS AND f_s OF DIFFERENT GCLLC-DCT TOPOLOGIES

Topology	C_{r1}(μF)	C_{r2}(μF)	f_s(kHz)
$g\to 0$	-	0.0057	96.6
$g=C_{st}$ ($C_{st}=2$)	0.0343	0.0172	95.3
$g\to\infty$	0.0227	-	96.3

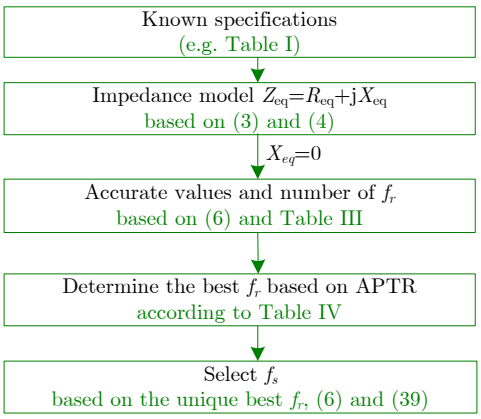

Fig. 16 Flowchart of the proposed three-step SFSC.

IV. EXPERIMENTAL VALIDATION

Based on the design example in Section III-D, the GCLLC-DCT prototype is developed and imbedded in a real hybrid AC/DC microgrid environment. As depicted in Fig. 17, a DC programmable source is used to simulate the PV energy. The DC and AC load banks are utilized to emulate different load profiles and load types. The HV side of DCT is connected to the DC output of BIC as shown in the figure to construct the AC sub-grid. BIC AC output is directly tied to AC programmable source, which simulates the utility grid. BIC is regulated by the DSPACE. The detailed experimental parameters of the GCLLC-type DCT are described in Table I and V.

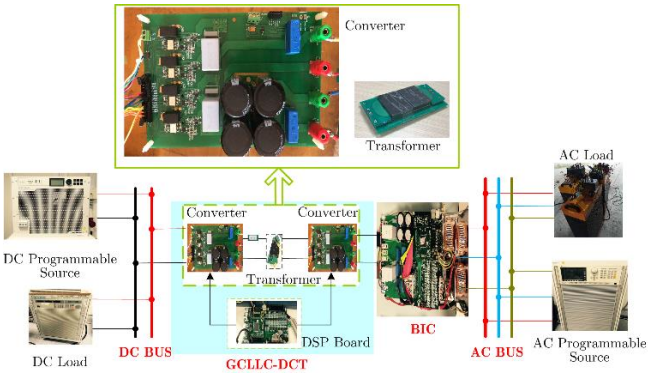

Fig. 17. GCLLC-DCT based hybrid AC/DC microgrid prototype.

A. Verification of PT ability in the GCLLC-DCT with the proposed SFSC

To verify the PT ability of the GCLLC-DCT achieved by the proposed SFSC, the experimental results have been measured in this sub-section when the power is transmitted from the HV side to the LV side.

- For the symmetric CLLC-DCT, the waveforms of the input voltage v_{in} and current i_{in} are given in Fig. 18. It can be observed the phase error between v_{in} and i_{in} is close to zero under both the light- and full-load conditions.
- For the asymmetric CLLC-DCT, the waveforms of v_{in} and i_{in} are similar to Fig. 18.
- For the CLL-DCT, the waveforms of v_{in} and i_{in} are depicted in Fig. 19. They are also kept in phase under both the light- and full-load conditions.
- For the LLC-DCT, the waveforms of v_{in} and i_{in} are similar to Fig. 19.

Since the efficiency directly reflects the APTR ability, the efficiency has been measured under both the light- and full-load conditions, as depicted Fig. 20. Apparently, the proposed SFSC exhibits satisfactory efficiency characteristics, especially during the light-load condition. If power is transferred from low voltage side to high voltage side, the similar results can be achieved.

In practice, the nonlinear relationship exists between g and efficiency, and this relationship may also change with power. Therefore, the efficiency of the symmetric CLLC-DCT at light-load condition outperforms that of the asymmetric CLLC-DCT, while at full-load condition it is the other way.

These results verify that the proposed SFSC overcomes the problems stated in Section II-B induced by the conventional f_s selection approach, and thus brings the good PT ability under both the light- and heavy-load conditions.

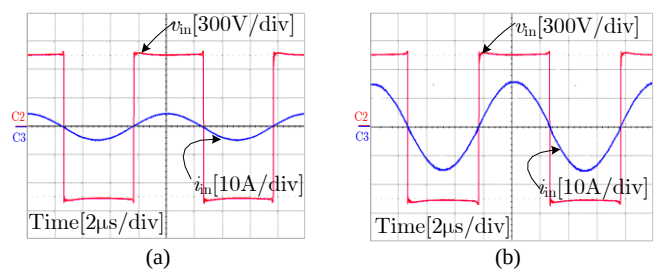

Fig. 18. Waveforms of v_{in} and i_{in}.(a) @ light-load condition and (b) @ full-load condition for the symmetric CLLC-DCT.

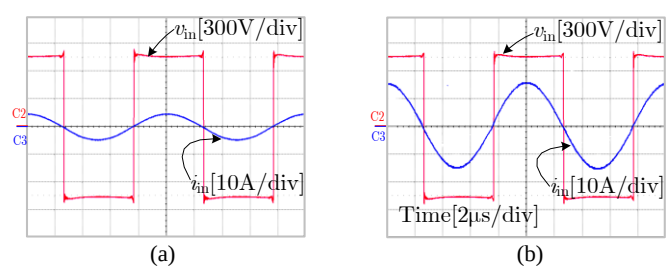

Fig. 19. Waveforms of v_{in} and i_{in}. (a) @light-load condition and (b) @ full-load condition for the CLL-DCT.

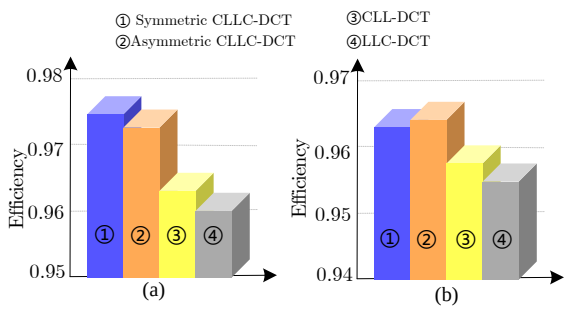

Fig. 20. Efficiency of the GCLLC-DCT: (a) at light-load condition and (b) at full-load condition.

B. Cooperation verification of the BIC and GCLLC-DCT

When the proposed SFSC is applied in the GCLLC-DCT to cooperate with BIC, the cooperation performance is verified in this sub-section. Since all the GCLLC-DCT topologies in Section IV-A guarantee the good PT ability, only the topology with g=1 is introduced here.

Fig. 21 shows the waveforms of the BIC and GCLLC-DCT when the power is transmitted from high voltage side to the low voltage side. Apparently, the AC current of BIC is controlled in phase with the corresponding AC voltage. Therefore, there is no reactive power transmission, effectively ensuring the power factor. Besides, the v_{in} and i_{in} of the GCLLC-DCT are also kept in phase, guaranteeing the PT ability.

When the bidirectional power transient occurs, the results are given in Fig. 22. It can be observed that the power transients can be smoothly completed within 10ms. Besides, during the steady state shown in Fig. 22, the total harmonic distortion (THD) of the AC current is less than 3.2%.

These experimental results further demonstrate the effectiveness of the proposed SFSC for GCLLC-DCT in the hybrid AC/DC microgrid application.

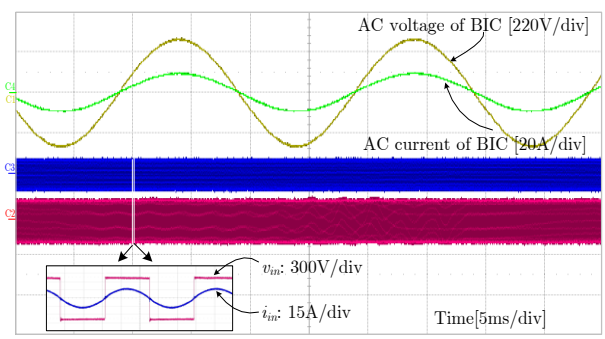

Fig. 21. Waveforms of GCLLC and DCT when the power is transmitted from high voltage side to the low voltage side of DCT.

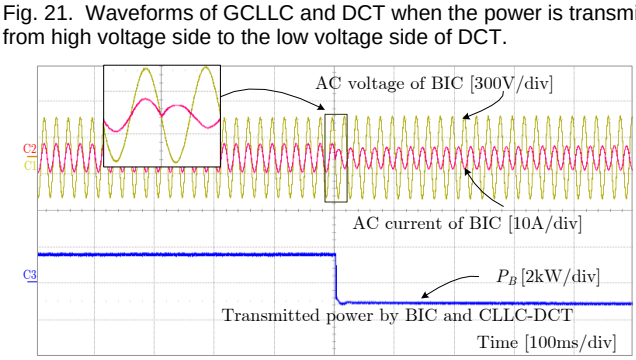

Fig. 22. Bidirectional power switching of the BIC and GCLLC-DCT.

V. Conclusion

Three-step switching frequency selection criteria have been proposed for the GCLLC-DCT to ensure the power transmission (PT) ability for cooperating with the BIC in the hybrid AC/DC microgrid application. The number, value and impact variables of the resonant frequency have been summarized as the preliminary to guide the future GCLLC-DCT design. Afterwards, both the optimum resonant and switching frequencies are determined to cope with the problems induced by the multiple resonant frequencies and the changing resonant parameters in practice. With the proposed SFSC, the GCLLC-DCT can guarantee the desired A_{PTR} with the highest probability. The proposed method has been validated by the experimental results.

Appendix

Note that (11a) is achieved by letting $X_{eq}(L_{r1}, L_{m1}, C_{r1}, \omega_s)\,|_{AB\to CD}=0$ to ensure the highest A_{PTR}, i.e.,

$$X_{eq}(L_{r1}, L_{m1}, C_{r1}, \omega_s)\,|_{AB\to CD} = \frac{L_{r1}^3 C_{r1}^2(\sigma_1\omega_s^6+\sigma_2\omega_1^2\omega_s^4+\sigma_3\omega_1^4\omega_s^2-\omega_1^6)}{\omega_s[\mathrm{R}_H^2\omega_s^2 g^2 C_{r1}^2+(\omega_s^2 g C_{r1}L_{r1}+\omega_s^2 g C_{r1}L_{m1}-1)^2]}=0 \tag{A1}$$

According to (A1), it can be derived that

$$\sigma_1\omega_s^6+\sigma_2\omega_1^2\omega_s^4+\sigma_3\omega_1^4\omega_s^2-\omega_1^6=0 \tag{A2}$$

By dividing ω_s^2 at both side of (A2), we can achieve that

$$F(\omega_s)=\underbrace{\sigma_1\omega_s^4+\sigma_2\omega_1^2\omega_s^2+\sigma_3\omega_1^4}_{y_1}-\underbrace{\omega_1^6/\omega_s^2}_{y_2}=0 \tag{A3}$$

Therefore, based on (A1) ~ (A3), eqn. (11a) can be achieved.

According to (10), the maximum value and minimum value of ω_1 defined as $\omega_{1\max}$ and $\omega_{1\min}$ respectively can be obtained as:

$$\omega_{1\max}=\frac{1}{\sqrt{(1-\zeta\%)(1-\xi\%)L_{r1R}C_{r1R}}}=\frac{\omega_{1D}}{\sqrt{(1-\zeta\%)(1-\xi\%)}} \tag{A4}$$

$$\omega_{1\min}=\frac{1}{\sqrt{(1+\zeta\%)(1+\xi\%)L_{r1R}C_{r1R}}}=\frac{\omega_{1D}}{\sqrt{(1+\zeta\%)(1+\xi\%)}} \tag{A5}$$

where ω_{1D} is expressed by

$$\omega_{1D}=1/\sqrt{L_{r1R}C_{r1R}} \tag{A6}$$

Therefore, eqn. (27) is achieved.

References

[1] J. Xiao, P. Wang, and L. Setyawan. "Hierarchical control of hybrid energy storage system in DC microgrids," *IEEE Trans. Ind. Electron.*, vol. 62, no. 8, pp. 4915-4924, Aug. 2015.

[2] X. Lu, K. Sun, J. Guerrero, J. Vasquez, and L. Huang. "State-of-Charge Balance Using Adaptive Droop Control for Distributed Energy Storage Systems in DC Microgrid Applications," *IEEE Trans. Ind. Electron.*, vol. 61, no. 6, pp. 2804-2815, June 2014.

[3] P. Wang, L. Goel, X. Liu, and F. Choo. "Harmonizing AC and DC: A hybrid AC/DC future grid solution," *IEEE Power Energy Mag.*, vol. 11, no. 3, pp. 76-83, May-June 2013.

[4] X. Zhang, Q. Zhong and W. Ming, "Stabilization of Cascaded DC/DC Converters via Adaptive Series-Virtual-Impedance Control of the Load Converter," in IEEE Transactions on Power Electronics, vol. 31, no. 9, pp. 6057-6063, Sept. 2016.

[5] X. Zhang, Q. Zhong, V. Kadirkamanathan, J. He and J. Huang, "Source-side Series-virtual-impedance Control to Improve the Cascaded System Stability and the Dynamic Performance of Its Source Converter," in IEEE *Trans. on Power Electronics*. 2018. doi: 10.1109/TPEL.2018.2867272.

[6] X. Zhang and Q. Zhong, "Improved Adaptive-Series-Virtual-Impedance Control Incorporating Minimum Ripple Point Tracking for Load Converters in DC Systems," in IEEE Transactions on Power Electronics, vol. 31, no. 12, pp. 8088-8095, Dec. 2016.

[7] Z. Ma, X. Zhang, J. Huang and B. Zhao, "Stability Constraining Dichotomy Solution Based Model Predictive Control to Improve the Stability of Power Conversion System in the MEA," in IEEE Transactions on Industrial Electronics. doi: 10.1109/TIE.2018.2875418.

[8] J. Huang, J. Xiao, C. Wen, P. Wang, and A. Zhang. "Implementation of Bidirectional Resonant DC Transformer in Hybrid AC/DC Micro-grid," *IEEE Trans. Smart Grid*, 2017, *DOI: 10.1109/TSG.2017.2771822*.

[9] J. Xiao, P. Wang, and L. Setyawan. "Implementation of multiple-slack-terminal DC microgrids for smooth transitions between grid-tied and islanded states," *IEEE Trans. Smart Grid*, vol. 7, no. 1, pp. 273-281, Jan. 2016.

[10] Y. Zheng, S. Li, and R. Tan. "Distributed model predictive control for on-connected microgrid power management," *IEEE Trans. Control Syst. Technol.*, vol. 26, no. 3, pp. 1028-1039, May 2018.

[11] M. Davari, and Y. Mohamed. "Robust multi-objective control of VSC-based DC-voltage power port in hybrid AC/DC multi-terminal micro-grids," *IEEE Trans. Smart Grid*, vol. 4, no. 3, pp. 1597-1612, Sept. 2013.

[12] S. Zhao, Q. Li, F. Lee, and B. Li. "High-Frequency Transformer Design for Modular Power Conversion from Medium-Voltage AC to 400 VDC,". *IEEE Trans. Power Electron.*, vol. 33, no. 9, pp. 7545-7557, Sept. 2018.

[13] B. Zhao, Q. Song, W. Liu, and Y. Sun. "Overview of dual-active-bridge isolated bidirectional DC–DC converter for high-frequency-link power-conversion system," *IEEE Trans. Power Electron.*, vol. 29, no. 8, pp. 4091-4106, Aug. 2014.

[14] R. Beiranvand, B. Rashidian, M. Zolghadri, and S. Alavi. "Using LLC resonant converter for designing wide-range voltage source," *IEEE Trans. Ind. Electron.*, vol. 58, no. 5, pp. 1746-1756, May 2011.

[15] W. Chen, P. Rong, and Z Lu, "Snubberless bidirectional DC-DC converter with new CLLC resonant tank featuring minimized switching loss," *IEEE Trans. Ind. Electron.*, vol. 57, no. 9, pp. 3075–3086, Sep. 2010.

[16] W. Malan, D. Vilathgamuwa, and G. Walker. "Modeling and control of a resonant dual active bridge with a tuned CLLC network," *IEEE Trans. Power Electron.*, vol. 31, no. 10, pp. 7297-7310, Oct. 2016.

[17] P. Wen, C. Hu, H. Yang, L. Zhang, C. Deng, Y. Li, and D. Xu. "A two stage DC/dc converter with wide input range for EV,"//*Power Electronics Conference (IPEC-Hiroshima 2014-ECCE-ASIA), 2014 International*, IEEE, 2014: 782-789.

[18] Z. Zhang, Y. Wu, D. Gu, and Q. Chen. "Current Ripple Mechanism with Quantization in Digital LLC Converters for Battery Charging Applications," *IEEE Trans. Power Electron.*, vol. 33, no. 2, pp. 1303-1312, Feb. 2018.

[19] G. Oggier, G. Garcia, and A. Oliva, "Modulation strategy to operate the dual active bridge dc-dc converter under soft switching in the whole operating range," *IEEE Trans. Power Electron.*, vol. 26, no. 4, pp. 1228-1236, Apr. 2011.

[20] D. Costinett, D. Maksimovic, and R. Zane, "Design and control for high efficiency in high step-down dual active bridge converters operating at high switching frequency," *IEEE Trans. Power Electron.*, vol. 28, no. 8, pp. 3931-3940, Aug. 2013.

[21] Y. Lo, C. Lin, M. Hsieh, and C. Lin. "Phase-shifted full-bridge series-resonant DC-DC converters for wide load variations," *IEEE Trans. Ind. Electron.*, vol. 58, no. 6, pp. 2572-2575, June 2011.

[22] J. Xiao, X. Bac, J. Huang, and Q. Zhou. "Implementation of DC/DC converter with high frequency transformer (DHFT) in hybrid AC/DC microgrid" //*Energy, Power and Transportation Electrification (ACEPT)*, 2017 Asian Conference on. IEEE, 2017: 1-5.

[23] J. Huang, X. Zhang, S. Zhu, Q. Zhou. "Dead-time effect on the CLLC-type DC transformer in hybrid AC/DC microgrid with 50% duty ratio control scheme," *2018 Chinese Control and Decision Conference (CCDC)*, IEEE, pp. 530-534, 2018.

[24] J. Huang, X. Zhang, Z. Shuai, X. Zhang, P. Wang, L. Koh, and X. Tong. "Robust Circuit Parameters Design for the CLLC-Type DC Transformer in the Hybrid AC/DC Microgrid," *IEEE Trans. Ind. Electron.*, vol. 66, no. 3, pp. 1906-1918, March 2018.

[25] H. Liu, Q. Liu, S. Zhou, C. Li, and S. Yuan. "A NURBS interpolation method with minimal feedrate fluctuation for CNC machine tools," *The International Journal of Advanced Manufacturing Technology*, vol. 78, no. 5-8, pp. 1241-1250, 2015.

Jingjing Huang (S'11–M'18) received the B.S. degree from the Henan University of Science and Technology, Luoyang, China, in 2008, and the Ph.D. degree from Xi'an Jiaotong University, Xi'an, China, in 2014, both in electrical engineering.

Since April 2014, she has been a Lecturer with the Xi'an University of Technology, Xi'an, China. Since December 2016, she has been a Research Fellow with Nanyang Technological University, Singapore. She has authored or co-authored over 60 technique papers. She holds more than 10 patents. Her research interests include renewable energy system, high-frequency transformer, hybrid ac/dc microgrid, and high-power converters.

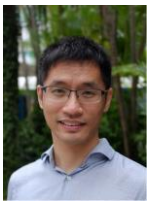

Xin Zhang (M'15) received the Ph.D. degree in automatic control and systems engineering from the University of Sheffield, Sheffield, U.K., in 2016, and the Ph.D. degree in electronic and electrical engineering from Nanjing University of Aeronautics and Astronautics, Nanjing, China, in 2014.

He is currently an Assistant Professor of power engineering with the School of Electrical and Electronic Engineering, Nanyang Technological University, Singapore. From January 2017 to September 2017, he was a Postdoctoral Research Fellow with the City University of Hong Kong. From February 2014 to December 2016, he was a Research Associate with the University of Sheffield. Dr. Zhang was the recipient of highly prestigious Chinese National Award for Outstanding Students Abroad in 2016.

Dr. Zhang services as the Associate Editors in IEEE TIE/JESTPE, IET Power Electronics. His research interests include power electronics, power systems, and advanced control theory, together with their applications in various sectors.

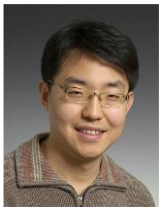

Zhe Zhang (M'11-SM'16) received the B.Sc. and M.Sc. degrees in power electronics from Yanshan University, Qinhuangdao, China, in 2002 and 2005, respectively, and the PhD degree from the Technical University of Denmark, Kgs. Lyngby, Denmark, in 2010.

He is currently an Associate Professor in the Department of Electrical Engineering, at the Technical University of Denmark (DTU). Since Jan. 2018, he has been Head of Studies in charge of Electrical Engineering MSc Programme, which is one of the largest MSc program at DTU. From 2005 to 2007, he was an Assistant Professor at Yanshan University. From June 2010 to August 2010, he was with the University of California, Irvine, CA, USA, as a visiting scholar. He was an Assistant Professor at the Technical University of Denmark during 2011 and 2014. He has authored or co-authored more than 130 transactions and international conference papers and filed 8 patent applications. He has supervised over 10 PhD students since 2013. Dr. Zhang's current research interests include applications of wide bandgap devices, high frequency dc-dc converters, multiple-input dc-dc converters, soft-switching power converters and multi-level dc-ac inverters for renewable energy systems (RES), hybrid electric vehicles (HEV) and uninterruptable power supplies (UPS); piezoelectric-actuator and piezoelectric-transformer based power conversion systems.

Dr. Zhang has received several awards and honors including Best Paper Award in IEEE ECCE, Best Paper Award in IEEE IGBSG, Best Teacher of the Semester, Chinese Government Award for Outstanding Students Abroad, etc. He is also a guest associate editor in IEEE Transactions on Industrial Electronics.